Modeling, experiments and optimization of an on-pipe thermoelectric generator

Jie Chen, Lei Zuo *, Yongjia Wu, Jackson Klein

Dept. Mechanical Engineering, Virginia Tech, Blacksburg, VA 24061, United States

ARTICLE INFO

ABSTRACT

A thermoelectric energy harvester composed of two thermoelectric modules, a wicked copper-water heat pipe, and finned heat sinks has been designed, modeled, and tested. The harvester is proposed to power sensor nodes on heating/cooling, steam, or exhaust pipes like these in power stations, chemical plants and vehicle systems. A model to analyze the heat transfer and thermoelectric performance of the energy harvesting system has been developed and validated against experiments. The results show that the model predicts the system power output and temperature response with reasonable accuracy. The model developed in this paper can be adapted for use with general heat sink, heat pipe, and thermoelectric systems. The design, incorporating a heat pipe and two 1.1″ by 1.1″ Bi$_2$Te$_3$ modules generates 2.25 W ± 0.13 W power output with a temperature difference of 128 °C ± 1.12 °C and source temperature of 246 °C ± 1.9 °C, which is more than enough to operate wireless sensors or some actuators. The use of a heat pipe in this design increased the power output by 6 times over conventional designs. Based on the model, further improvement of the power output and energy harvesting efficiency of the system has been suggested by optimizing the number of thermoelectric modules.

1. Introduction

A thermoelectric module is a solid-state heat engine consisting of multiple P/N legs connected electrically in series and thermally in parallel. Modules are mechanically simple enabling them to operate quietly and stably over long lifetimes. This gives them a significant advantage over conventional heat engines for specific applications, even though their efficiency is low due to their figure of merit (ZT) [1]. Traditionally, thermoelectric generators (TEGs) have been used in aeronautical engineering, military, and medical fields. However, with the rapid development of nanotechnology, new materials with higher efficiency and special characteristics have been discovered, broadening the applications of TEGs. Recent designs include wearable TEGs for powering small carry-on electronics, solar thermoelectric energy harvesting, and automobile exhaust pipe energy scavenging [2–4]. In order to advance the field, this paper investigates a simple, versatile thermoelectric based energy harvester built to utilize thermal energy from high temperature pipes and exhausts as are found in power stations, chemical plants, and transportation systems.

There have been extensive studies on harvesting energy from high temperature pipes. The first attempt to harvest energy from an exhaust pipe using a TEG was in 1963 [5]. Since then, Haidar and Jamil [6] built a TEG system with commercially available Bi$_2$Te$_3$ modules, in which an aluminum spreader block was designed to mount modules on an exhaust pipe. This system generated a maximum power of 12.2 W under a temperature difference of 237 °C using four modules with 2″ × 3″ surface area. Ikoma et al. [7] developed a SiGe module with eight pairs of legs for use in an elevated temperature, and applied it to a generator system with a heat exchanger on a rectangular exhaust pipe. Using 72 modules, they obtained a maximum power of 35.6 W with a 563 °C temperature difference. Hsu et al. [8,9] developed two generations of exhaust-based thermoelectric generators, and conducted an extensive study on system performance in low-temperature range with prototypes. Goncalves et al. [10] and Martins et al. [11] proposed a heat pipe assisted thermoelectric generator design, which included multiple heat pipes to absorb heat from an exhaust pipe and transport it to the hot end of thermoelectric modules (TEMs). Dell et al. [12] constructed a prototype that can be implemented onto steam pipes robustly. Using six Bi$_2$Te$_3$ thermoelectric modules with 1.57″ by 1.73″ surface area, the approximate power output is 6.9 W at a temperature gradient of 63 °C. Tewolde et al. [13] proposed a design that could be directly mounted onto the outer surface of a steam pipe, producing a matched load power of 1.0 W during real application. However, there still has been a lack of research done on steam pipe thermal energy harvesting. To address this problem,

Nomenclature

A	surface area (m^2)
$C_1 \sim C_4$	constants
h	convective heat transfer coefficient (W m^{-2} K^{-1})
I	current (A)
k	thermal conductivity (W m^{-1} K^{-1})
K	thermal conductance (W K^{-1})
$\overline{K}$	thermal conductance mean value (W K^{-1})
L	length (m)
m	total number of exposed surfaces
n	total number of leg pairs in two TEMs
N	total number of TEM at each side
Nu	Nusselt number
P	power output (W)
Pr	Prandtl Number
q	heat flux (W m^{-2})
Q	overall heat (W)
r	radius (m^2)
R	thermal resistance (K W^{-1}); electrical resistance (Ω)
$\overline{R}$	electrical resistance mean value (Ω)
Re	Reynold's number
t	thickness (m)
T	temperature (K)
ΔT	temperature difference (K)
V	voltage (V)
W	width (m)

Greek symbols

α	seebeck coefficient (V/K)
$\bar{\alpha}$	seebeck coefficient mean value (V/K)
ϵ	aspect ratio
ε	surface emissivity
σ	Stefan-Boltzmann constant (W m^{-2} K^{-4})
η	system efficiency

Subscripts

a	adiabatic section
amb	ambient
b	base plate of heat sink
c	cold side of TEM leg
co	condenser
cv	convection
C	cold side of TEM
ce	ceramic
D	pipe diameter
e	evaporator
ex	external surface
f	fin area
h	hot side of TEM leg
H	hot side of TEM
hp	heat pipe
hs	heat sink
i	exposed surfaces
in	internal material of TEM
los	loss
L	load at external side
N	N-type leg
o	open circuit
p	adaptor plate
pr	primary area in heat sink
P	P-type leg
PN	PN pair
r	radiation
sp	spreading
S	source
$tg1 \sim tg4$	thermal grease layers
TEM	thermoelectric module
$0 \sim 10$	different sections in heat pipe

the presented novel system is able to provide enough power for wireless sensing and monitoring systems within power plants. It is easily integrated, and highly adaptable for any high temperature pipe installation.

To predict thermoelectric energy harvesting systems performances, many studies have been published regarding the mathematical modeling of these systems [14–18]. The thermoelectric process is indeed coupled by heat conduction, the Peltier Effect, the Thomson Effect, and Joule Heating. The conventional 1-D model [16] is the most commonly used, in which a constant heat flow is assumed. However, it is not accurate enough due to its neglect of the energy conversion process. Zhao and Tan [14] summarized the current materials, modeling methods, and applications of thermoelectric generators. Fraisse et al. [15] summarized the prevailing modeling techniques for thermoelectric processes based on an order of complexity, and compared the accuracy of all models. Thermos-pellets are the core component in a TE module, and Sahin and Yilbas [19] studied the influence of thermos-pellet geometry on the performance of the device. They indicated that trapezoid shape could improve the efficiency but reduce the power generation. Chen et al. [20] performed an optimization towards a two-stage thermoelectric generator by searching for the optimal heat transfer surface and the pair numbers using non-equilibrium thermodynamics and finite-time thermodynamics.

There have been several mathematical models made for integrated designs of specific applications [21–23]. In the simplest case, researchers do not consider the fact that energy conversion within the module may cause a large deviation in performance

anticipation [16]. Many existing models do not take into account the impact of sealing material (gas gap between thermos-pellets in the TE modules) in the TE modules, which can reduce the efficiency and power output of the system. Finally, the variation of the thermal resistance of heat sinks with temperature and heat flow through them is generally over-looked. Hsiao et al. [21] investigated the detailed mathematical modeling techniques for waste heat recovery from automobile engines based on a design integrating two heat sinks, in which they treated the thermal resistance of heat sinks as constant. However, due to a reduction in accuracy, this should not be treated as a constant. Gou et al. [22] conducted modeling and an experimental study on a design targeting for harvesting energy from a flow channel, and optimized the design by enhancing heat transfer capacity at the cold side.

The modeling addressed here is of a thermoelectric energy harvesting system used to extract energy from a high-temperature pipeline (Fig. 1) in order to power a wireless sensing and monitoring system. A heat pipe was chosen for its excellent thermal conductivity in order to conduct heat out of insulation layer through a penetrated (Fig. 1a) or unpenetrated (Fig. 2b) connection. A lab-based experiment was carried out to test the characteristics of the system, and validate the modeling.

In the following sections, the prototype is described, and a highly applicable model is constructed, which combines the coupled effects of heat sink thermal resistance, energy conversion, and sealing material in commercial TEG modules on system performance. This model agrees with lab based experimental tests of the prototype with promising accuracy, and an optimization of the
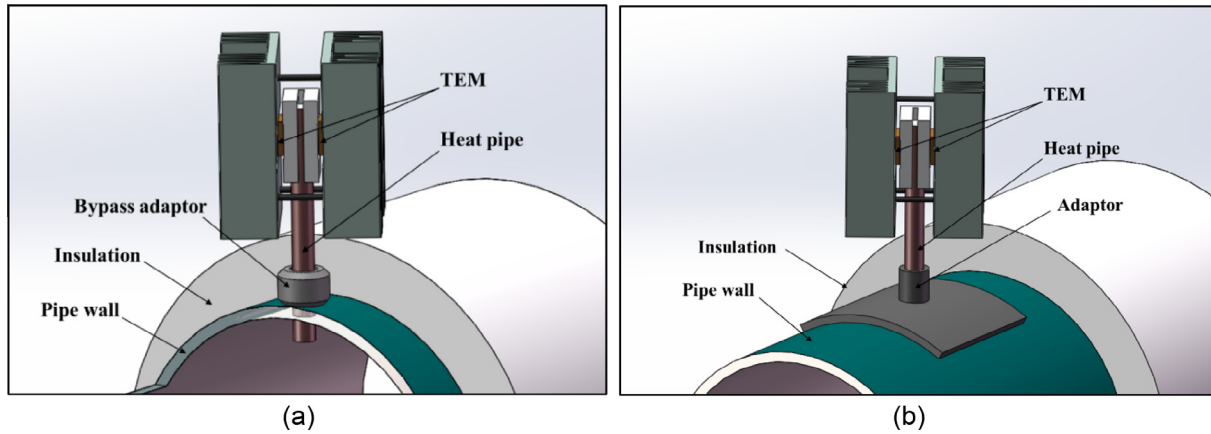
Fig. 1. Heat pipe-assisted TEG for on-pipe energy harvesting: (a) penetrated design and (b) unpenetrated design.
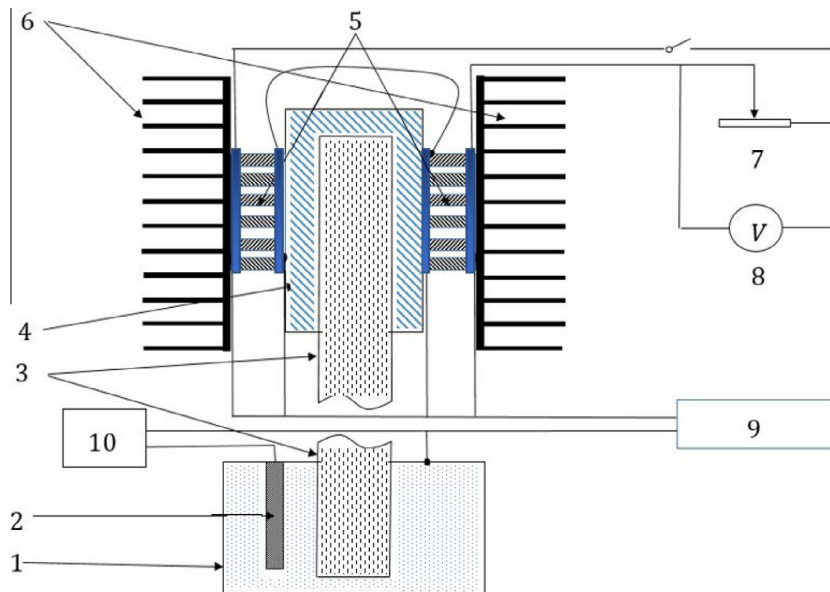

Fig. 2. Schematic diagram of thermoelectric generator experimental setup. 1: Heat source block. 2: Cartridge heater. 3: Heat pipe. 4: U shape hot side coupler. 5: Thermoelectric modules. 6: Heat sinks. 7: Electrical load. 8: Voltage reading DAQ. 9: K type thermocouples and temperature reading DAQ. 10: PID heater controller.

energy harvesting system was carried out using the model in order to guide the improvement of the system for future work. By adding thermoelectric modules, the performance of this prototype can further increased.

2. Design and experiment setup

The presented system harvests energy from high temperature fluid pipelines in order to power increasingly necessary wireless sensor nodes in power stations, chemical plants, and transportation systems. Such pipelines usually have a thick thermal insulation layer, thus, as illustrated in Fig. 1, the prototype places TEG modules and heat sinks outside the thermal insulation for easy maintenance. In order to achieve this unique aspect of the design, a heat pipe is used to conduct heat from the high temperature fluid pipelines to the TEGs. By combining the principles of both thermal conductivity and phase transition, the heat pipe has an equivalent thermal conductivity many times more than that of copper and aluminum. The high temperature end of the heat pipe can be mounted on the fluid pipe with an adapter or through penetration.

The prototype, and experimental setup is shown in Fig. 2. Two 1.1″ by 1.1″ Bi_2Te_3 thermoelectric modules (Hz-2 from Hi-z Technology California with the working temperature range of 30–250 °C) were implemented electrically in series and thermally in parallel. The geometric and transport properties of the Hz-2 module are listed in Table 1. A wicked copper-water heat pipe manufactured by Noren Products Inc. was selected for heat transfer to the TEMs. This heat pipe has a suggested maximum temperature of 600 °F, is 200 mm (7.88″) long, 19.05 mm (0.75″) in diameter and has a porosity of 0.5. The thickness of the copper layer is about 0.5 mm, and the thickness of wick layer is around 1.2 mm. Determined by this specific application and design, the evaporator and condenser sections are 50 mm and 60 mm respectively. Two aluminum heat sinks from ABL Heatsinks are implemented on the cold side of each TEM to dissipate heat through natural convection. Each heat sink has an overall size of 125 mm (width) × 150 mm (length) × 50 mm (height), and 10 fins with an average fin space of 5.5 mm and fin height of 41 mm. For lab based test purposes, a brass block 30 mm (width) × 50 mm (length) × 60 mm (height) in size was used as a heat source. A 200 W cartridge heater (CIR-10151, OEMGA Engineering) and a temperature controller

Table 1
Geometric parameters and transport properties of the Hz-2 module [24].

Parameters	N-type leg	P-type leg	Aluminum	Insulating ceramic
Seebeck coefficient (V/K)	-1.77×10^{-4}	2.01×10^{-4}	N/A	N/A
Thermal conductivity (W/(m K))	1.054	1.373	205	1.74
Electrical resistivity (Ω m)	1.53×10^{-5}	1.53×10^{-5}	2.7×10^{-8}	N/A
Cross section area (m^2)	2.31×10^{-6}	2.31×10^{-6}	5.29×10^{-6}	6.17×10^{-6}
Thickness (m)	2.98×10^{-3}	2.98×10^{-3}	1.09×10^{-3}	2.98×10^{-3}

(CN7800, OMEGA Engineering) were used to control the source temperature during the experimental process. The block has a heating distance (cartridge heater to heat pipe) of 12.7 mm. For the power measurement, a series of electrical resistors were connected as external loads. Five K type thermocouples with an error of 0.75% were used. Two were placed between the hot side adaptor and TEG modules, within the thermal grease layer, two were placed in the thermal grease layer between the TEG modules and the heat sinks, and finally one was placed in the heater block for source temperature. Each of these can be seen as 9 in Fig. 2. Two DAQs from National Instruments Inc, NI TB-9214 (with an accuracy of 0.45 °C) and NI USB 6008 (with an accuracy of 7.7 mV), were used to collect the temperature and voltage readings of the system separately.

3. Analytical modeling

A comprehensive modeling of the previously described thermoelectric energy harvesting system is presented in this section. It includes the thermoelectric modules, the temperature-dependent thermal resistance of heat sinks, the wicked heat pipe, the adapters and heat loss through radiation and convection. Later, a comparison is made between the model prediction and experimental results. The modeling can easily be adapted to any general thermoelectric based energy harvester.

3.1. System heat transfer and thermal resistances

Considering the primary application of this system is to harvest energy from high-temperature water or steam loops where the source temperature can be treated as constant, the modeling of

the heat transfer process was performed in steady state. Therefore, a thermal network is built where the thermal resistance of each element is analyzed in steady state. As shown in Fig. 3(a), the thermal circuit consists of six elements: heat source, heat pipe, hot side block, TE modules, heat sinks, and the contact at each interface. Here the thermal resistance of each TEM is not taken as passive, but will be discussed in detailed later. Among all the elements in the heat transfer model, resistances of the source, heat pipe, and heat sinks vary in different working conditions.

For a penetration design (Fig. 1a), heat is transferred to the heat pipe through convection by the high temperature fluid at the external surface of evaporator. The equivalent thermal resistance is given by

$$R_s = \frac{1}{h_{ex} A_{ex}} \tag{1}$$

where h_{ex} is the convective heat transfer coefficient, which can be calculated by using the average Nusselt number Nu_D, i.e. $h_{ex} = \frac{\overline{Nu_D} k_s}{D}$, where k_s is thermal conductivity of source fluid. The Nusselt number of a cross flow past a perpendicular cylinder is (as presented in [10])

$$\overline{Nu_D} = 0.3 + \frac{0.62 Re_D^{0.5} Pr^{0.33}}{\left[1 + \left(\frac{0.4}{Pr}\right)^{0.67}\right]^{0.25}} \left[1 + \left(\frac{Re_D}{282000}\right)^{0.625}\right]^{0.8} \tag{2}$$

where Re_D is the Reynolds number; Pr is the Prandtl number.

The detailed modeling of the thermal resistance of each element inside a heat pipe can be found in [25,26]. In this work, applying the steady state assumption avoids the discussion of heat transfer in transient state. The thermal resistances of all elements in a heat pipe along the heat transfer path are denoted as follows: the
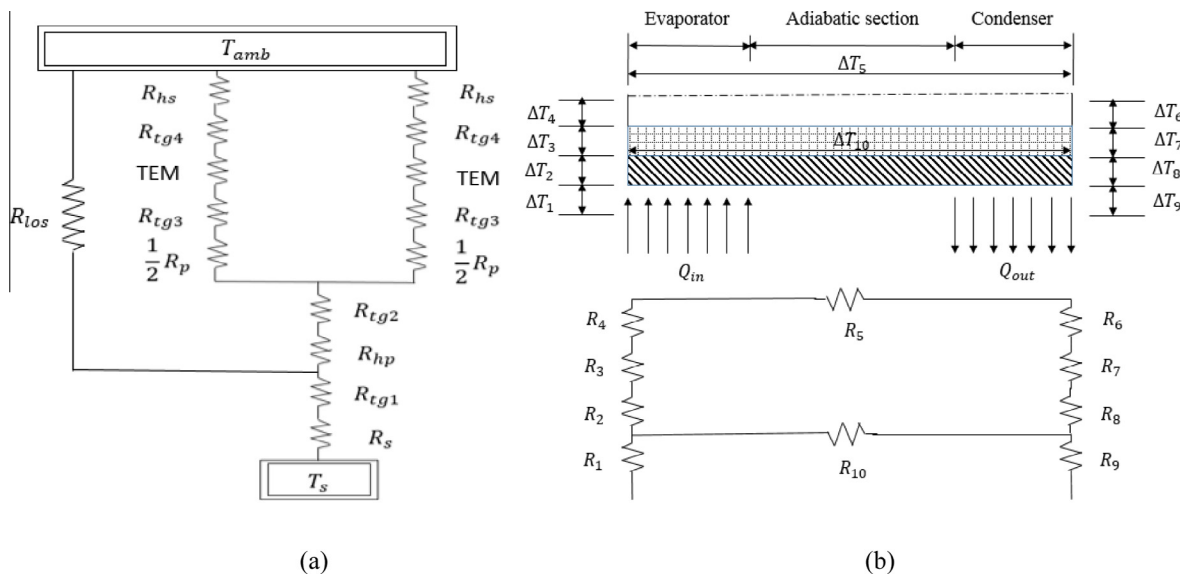
Fig. 3. Schematic diagram of the heat transfer circuit model for the overall design (a) and thermal resistances in a heat pipe (b) [25]. R_s: resistance of source. R_{hp}: heat pipe resistance. R_p: adaptor thermal resistance. TEM: thermoelectric module resistance. R_{hs}: heat sink resistance. R_{tg}: contact resistance at interfaces with thermal grease. R_{los}: heat loss.

Table 2
Specification of heat pipe interior resistance in this model.

Thermal resistances inside the heat pipe [25]	Calculated values(K/W)
$R_2 = \frac{\log(r_0/r_2)}{2\pi k_2 L_e}$	4×10^{-4}
$R_3 = \frac{\log(r_2/r_3)}{2\pi k_3 L_e}$	0.016
R_4, R_5, R_6	Negligible
$R_7 = \frac{\log(r_2/r_3)}{2\pi k_3 L_{co}}$	5×10^{-4}
$R_8 = \frac{\log(r_0/r_2)}{2\pi k_2 L_{co}}$	0.019
$\frac{1}{R_{10}} = \frac{1}{[L_a + 0.5(L_e + L_{co})]/k_2 \pi(r_0^2 - r_2^2)} + \frac{1}{[L_a + 0.5(L_e + L_{co})]/k_3 \pi(r_2^2 - r_3^2)}$	$\frac{1}{14.416}$

conductive resistance in the evaporator side wall and wick layer (R_2, R_3), the evaporating resistance at hot side wick surface (R_4), resistance due to mass transfer (R_5), the condensing resistance at cold side wick surface (R_6), the conductive resistance in the condenser side wall and wick layer (R_7, R_8), and the axial conductive resistance in wall and wick layer (R_{10}). R_1 and R_9 are the resistances on the outer surface, which depend on the connection type and will be counted in later sections. A detailed heat transfer circuit for the heat pipe is shown in Fig. 3(b). The specific items of the heat pipe interior resistance are listed in Table. 2. The overall thermal resistance of heat pipe is

$$R_{hp} = \left(\frac{1}{R_{10}} + \frac{1}{\sum_{i=2}^{8} R_i} \right) \tag{3}$$

The calculated result of the overall thermal resistance of the heat pipe used in the experimental prototype is 0.035 K/W.

The thermal resistance of each heat sink is comprised of three parts: conductive resistance at the base plate, spreading resistance at the base plate, and convectional and conductive resistances at the fins [27]. The base resistance is

$$R_b = \frac{t_b}{k_b A_b} = \frac{t_b}{k_b(W_b L_b)} \tag{4}$$

The spreading resistance is due the change of surface area along the heat flow path, given in [28], is:

$$R_{sp} = \frac{1 - 1.410\epsilon + 0.344\epsilon^3 + 0.043\epsilon^5 + 0.034\epsilon^7}{4k_b \sqrt{A_{TEM}}} \tag{5}$$

where ϵ is the ratio of the beginning and ending surface areas.

The thermal resistance at the fins includes conductive, convective, and radiative resistances inside the cooling channels. For this heat sink, an overall thermal resistance at the fins is [29]:

$$R_f = \frac{1}{(h_{cv} + h_r)(A_{pr} + \eta_f A_f)} \tag{6}$$

where A_{pr} and A_f are primary plate area and fin area, respectively; η_f is the fin efficiency, h_{cv} and h_r are the convective and radiative heat transfer coefficients, whose values are all temperature dependent. Therefore, an iteration is needed to determine the thermal resistance of the heat sinks under different fin surface temperature. Detailed calculation of R_{fa} can be found in [28,30].

The overall thermal resistance at the heat sink side is:

$$R_{hs} = R_b + R_{sp} + R_f \tag{7}$$

In this design and prototype, thermal grease was evenly applied on each contact surface. Therefore, contact resistance of each surface is modeled as a thin layer of thermal grease with a uniform thickness based on the surface roughness and tolerance. The thermal grease (OT-201, OMEGA Engineering) has a conductivity of 2.3 W/(m K). For contact resistances at both TEM ends, R_{tg3} and R_{tg4}, the average thickness of thermal grease is 0.45 mm due to the installation of thermocouples.

The heat loss through exposed surfaces of the heat pipe and aluminum block has significant impact on the system performance in high temperature conditions. Since the thermal resistances of the heat pipe, and interfaces at both ends of the heat pipe are smaller compared to those in each TE module, the temperatures at each exposed surface are close to the source temperature at the heat pipe evaporator side. Thus, the radiative and convective heat loss on those surfaces are calculated based on the source temperature. The total heat loss is

$$Q_{los} = K_{los}(T_s - T_{amb})$$
$$= \sigma\varepsilon(T_s^4 - T_{amb}^4)\sum_{i=1}^{m} A_i + (T_s - T_{amb})\sum_{i=1}^{m} h_i A_i \tag{8}$$

where the first term refers to the summed radiative heat loss at all surfaces, and the second term refers to the summed convective heat loss at all surfaces. Due to the different geometry of the surfaces, the convective coefficient h_i varies at each surface [31].

3.2. Modeling of thermoelectric modules

The physical principals dominating operation of a pair of positive (P-type) and negative (N-type) thermoelectric legs consist of five parts: heat conduction, Joule Heating, the Seebeck Effect, Peltier Cooling/Heating, and the Thomson Effect [32]. The Seebeck Effect indicates that an electric voltage is produced when the two ends are subjected to a temperature difference.

$$V = n\alpha(T_h - T_c) = n\alpha \, \Delta T \tag{9}$$

Here $\alpha = \alpha_P - \alpha_N$, and α_P and α_N represent the Seebeck coefficients of positive and negative legs, respectively. In this application, the Thomson Effect is neglected since the temperature gradient is not large and its impact on the overall assembly is much smaller than its impact on the TE module [33].

To harvest energy, an external load R_L is needed. The electrical current in the circuit will be

$$I = \frac{n\alpha\Delta T}{R_{in} + R_L} \tag{10}$$

where R_{in} is the internal electrical resistance of the module which can be calculated through material electrical conductivity and leg geometry. The diagram of energy harvesting and heat transfer processes in a commercial TEG is shown in Fig. 4.

The overall thermal resistance of a TEG is effected by five layers: electrical insulation and aluminum connector layers on either side of the module, and the functional semiconductor middle layer. Due to a large difference in the thermal conductance of aluminum and semiconductor materials, the temperature difference across the aluminum/insulator layers can be neglected.

The thermal resistance of sealing materials, typically ceramic and polymers used to protect thermoelectric legs, is considered in this modeling. The thermal conductance at the hot side, K_H, is the summed conductance of all elements in the heat flow path from source to the hot side of a P/N leg, as stated in Eq. (11). The conductance at cold side, K_C is the summed conductance of the heat sink and thermal grease, as shown in Eq. (12).

$$\frac{1}{K_H} = R_s + R_{tg1} + R_{hp} + R_{tg2} + \frac{1}{2}\left(\frac{1}{2}R_p + R_{tg3}\right) \tag{11}$$

$$\frac{1}{K_C} = \frac{1}{2}(R_{tg4} + R_{hs}) \tag{12}$$

Inside the thermoelectric module, the thermal conductance is composed of K_{PN} and K_{ce}, which are the thermal conductances of P/N pairs and the insulating ceramic respectively. The summed thermal conductance of one pair of legs, and the sealing material is
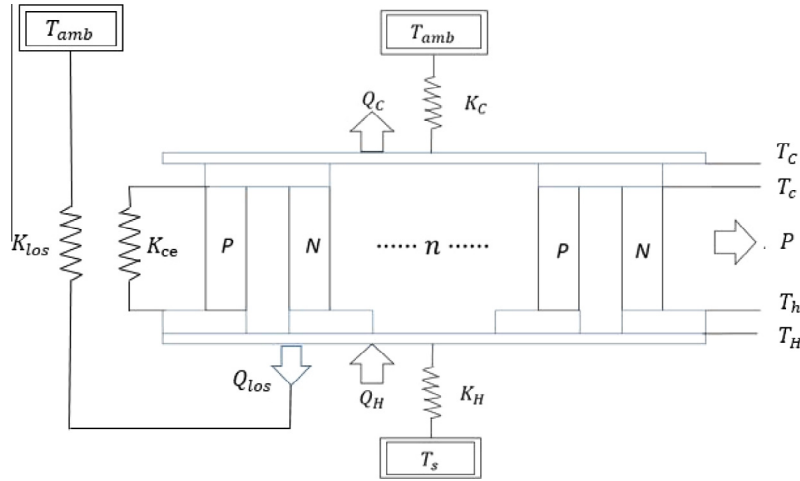
Fig. 4. Schematic diagram of heat transfer and energy conversion in a typical thermoelectric module.

$$K_{PN} = \frac{k_P \cdot A_P}{L_p} + \frac{k_N \cdot A_N}{L_N} \tag{13}$$

$$K_{ce} = \frac{k_{ce}(A_{TEM} - nA_P - nA_N)}{L_{ce}} \tag{14}$$

where k_P, k_N and k_{ce} are the thermal conductivity of P-type, N-type legs and sealing material, respectively. L_P and L_N are the leg heights where $L_P = L_N = L_{ce}$; A_{TEM}, A_N, and A_p are the cross sectional area of the module and the legs from which the cross section area of ceramic insulation can be found.

The internal electrical resistance of a TEG mainly comes from the semi-conductive thermoelectric legs in series.

$$R_{in} = n\left[\frac{\rho_P \cdot L_P}{A_p} + \frac{\rho_N \cdot L_N}{A_N}\right] \tag{15}$$

The rates of incoming heat and removal heat at the hot and cold junction of a single pair are

$$q_h = \bar{\alpha}IT_h - \overline{K}_{PN}(T_h - T_c) + \frac{1}{2}I^2\overline{R}_{PN} \tag{16}$$

$$q_c = \bar{\alpha}IT_c - \overline{K}_{PN}(T_h - T_c) - \frac{1}{2}I^2\overline{R}_{PN} \tag{17}$$

where $\bar{\alpha}$ is the Seebeck coefficient at the mean temperature of both sides, and $\overline{K}_{PN}$ and $\overline{R}_{PN}$ are the conductance and electrical resistance of a pair at the mean temperature. Let $\bar{\alpha} = \alpha = \frac{\alpha_P + \alpha_N}{2}$, $\overline{K}_{PN} = K_{PN}$ and $\overline{R}_{PN} = R_{PN}$. According to the energy conservation law, the governing equations at the hot and cold side of module [21], and the heat balance equation at ceramic insulation are

$$nq_h + q_{ce} = K_H(T_s - T_h) - K_{los}(T_h - T_{amb}) \tag{18}$$

$$nq_c + q_{ce} = K_C(T_c - T_{amb}) \tag{19}$$

$$q_{ce} = K_{ce}(T_h - T_c) \tag{20}$$

By substituting Eqs. (16) and (17) into Eqs. (18)–(20), the hot side and cold side temperature can be determined in terms of known variables, T_s, T_{amb} and I.

$$T_h = \left[\frac{1}{2}\alpha n^2 I^3 R_{PN} - \left(\frac{1}{2}nK_C + n^2K_{PN} + nK_{ce}\right)I^2 R_{PN}\right.$$
$$+ n\alpha I(K_H T_s - K_{los}T_s + K_{los}T_{amb}) - (nK_{PN} + K_{ce})(K_H T_s + K_C T_{amb})$$
$$\left. - K_H K_C T_s - K_C K_{los}T_s + K_C K_{los}T_{amb}\right] \times [n^2\alpha^2 I^2 + n\alpha(K_H - K_C)I$$
$$- (nK_{PN} + K_{ce})(K_H + K_C) - K_H K_C]^{-1} \tag{21}$$

$$T_c = -\left[\frac{1}{2}\alpha n^2 I^3 R_{PN} + \left(\frac{1}{2}nK_H + n^2 K_{PN} + nK_{ce}\right)I^2 R_{PN}\right.$$
$$+ n\alpha I(K_C T_{amb} + K_{los}T_s - K_{los}T_{amb})$$
$$+ (nK_{PN} + K_{ce})(K_H T_s + K_C T_{amb}) + K_H K_C T_{amb}$$
$$\left. + K_H K_{los}T_s - K_H K_{los}T_{amb}\right] \times [n^2\alpha^2 I^2 + n\alpha(K_H - K_C)I$$
$$- (nK_{PN} + K_{ce})(K_H + K_C) - K_H K_C]^{-1} \tag{22}$$

By substituting Eqs. (21) and (22) into Eqs. (17) and (18), the heat flow in and out the thermoelectric module is

$$Q_h = K_H(T_s - T_h)$$
$$= [\alpha n^2 K_H R_{PN}I^3 - nK_H(2n\alpha^2 T_s + 2nK_{PN}R_{PN} + K_C R_{PN} + 2K_{ce}R_{PN})I^2$$
$$- 2n\alpha K_H(K_C T_s - K_{los}T_s + K_{los}T_{amb})I$$
$$+ 2K_H K_C(nK_{PN} - K_{los} + K_{ce})(T_s - T_{amb})]$$
$$\times [-2n^2\alpha^2 I^2 - 2n\alpha(K_H - K_C)I + 2(nK_{PN} + K_{ce})(K_H + K_C) + 2K_H K_C]^{-1} \tag{23}$$

$$Q_c = K_C(T_c - T_{amb})$$
$$= [\alpha n^2 K_C R_{PN}I^3 + nK_C(2nK_{PN}R_{PN} + 2n\alpha^2 T_{amb} + K_H R_{PN}$$
$$+ 2K_{ce}R_{PN})I^2 + 2n\alpha K_C(K_H T_{amb} - K_{los}T_{amb} + K_{los}T_s)I$$
$$+ 2K_H K_C(nK_{PN} + K_{los} + K_{ce})(T_s - T_{amb})]$$
$$\times [-2n^2\alpha^2 I^2 - 2n\alpha(K_H - K_C)I + 2(nK_{PN} + K_{ce})(K_H + K_C) + 2K_H K_C]^{-1} \tag{24}$$

By subtracting Eq. (21) by Eq. (22) and combining Eq. (10), the temperature difference across the module, ΔT, in terms of system input variables, T_s and R_L, is found from

$$C_1(\Delta T)^3 + C_2(\Delta T)^2 + C_3\Delta T + C_4 = 0 \tag{25}$$

where

$$C_1 = \frac{n^4\alpha^4}{(nR_{PN} + R_L)^2} - \frac{\alpha^4 n^5 R_{PN}}{(nR_{PN} + R_L)^3}$$

$$C_2 = -\frac{\alpha^2 n^3 R_{PN}(K_H - K_C)}{2(nR_{PN} + R_L)^2} + \frac{\alpha^2 n^2(K_H - K_C)}{nR_{PN} + R_L}$$

$$C_3 = -\frac{\alpha^2 n^2(K_H T_s + K_C T_{amb})}{nR_{PN} + R_L} - (nK_{PN} + K_{ce})(K_H + K_C) - K_H K_C$$

$$C_4 = [K_H K_C - K_{los}(K_H - K_C)](T_s - T_{amb})$$

This equation can be solved to derive the closed form solution for T_s and ΔT. Due to its complexity, the exact closed form solution is not displayed here. The first term in Eq. (25) is negligible compared to the other three terms, therefore, ΔT is subjected to a quadratic distribution with respect to source temperature. The second term is also small in low temperature range, which leads to an almost linear relation between ΔT and T_s.

The current can be calculated using Eq. (10); the voltage and power generated on the resistive load can be calculated using $V_L = IR_L$ and $P = I^2 R_L$, respectively.

3.3. System performance prediction and optimization

Using T_h, T_c, Q_h and Q_c, and ignoring any heat loss, the closed form solutions for the open circuit voltage (without external load), power output, and the efficiency with external load in terms of T_s, T_{amb} and I are

$$
\begin{aligned}
V_O &= n\alpha(T_h - T_c) \\
&= [\alpha^2 n^3 I^3 R_{PN} + \alpha n^2 I^2 R_{PN}(K_H - K_C)/2 + n^2\alpha^2 I(K_H T_s \\
&\quad + K_C T_{amb}) - n\alpha K_H K_C(T_s - T_{amb})] \\
&\quad \times [n^2\alpha^2 I^2 + n\alpha(K_H - K_C)I - (nK_{PN} + K_{ce})(K_H + K_C) - K_H K_C]^{-1}
\end{aligned}
\tag{26}
$$

$$
\begin{aligned}
P &= n\alpha I(T_h - T_c) - nI^2 R_{PN} \\
&= \{-\alpha n^2 R_{PN}(K_H - K_C)I^3 + 2[n^2\alpha^2(K_H T_s + K_C T_{amb}) + nR_{PN}(nK_{PN} \\
&\quad + K_{ce})(K_H + K_C) + nR_{PN}K_H K_C]I^2 - 2n\alpha K_H K_C(T_s - T_{amb})I\} \\
&\quad \times [2n^2\alpha^2 I^2 + 2n\alpha(K_H - K_C)I - 2(nK_{PN} + K_{ce})(K_H + K_C) - 2K_H K_C]^{-1}
\end{aligned}
\tag{27}
$$

$$
\begin{aligned}
\eta &= 1 - Q_c/Q_h \\
&= \{-\alpha n^2 R_{PN}(K_H - K_C)I^3 - [2n^2\alpha^2(K_H T_s + K_C T_{amb}) \\
&\quad + 2nR_{PN}(K_H + K_C)(nK_{PN} + K_{ce}) + 2nR_{PN}K_H K_C]I^2 \\
&\quad - 2n\alpha K_H K_C(T_s - T_{amb})I\} \times [\alpha n^2 K_H R_{PN} I^3 \\
&\quad - 2nK_H(n\alpha^2 T_s + nK_{PN}R_{PN} + K_C R_{PN}/2 + K_{ce}R_{PN})I^2 \\
&\quad + 2n\alpha K_H K_C T_s I + 2K_H K_C(nK_{PN} + K_{ce})(T_s - T_{amb})]^{-1}
\end{aligned}
\tag{28}
$$

Eqs. (26)–(28) provide direct interrelation between output and input parameters of this coupled system. The output voltage, power, and working efficiency can now be evaluated in terms of system inputs and manipulated by changing the design. An optimization technique for this application can be implemented by adding more modules or using different external electrical loads, the number of legs and current can be manipulated. The reason to add modules on both sides simultaneously is to ensure the heat transfer circuit is parallel and thus the modeling above can be applied.

4. Results and discussion

4.1. TEG system performance and model validation

Given the algorithm specifying thermal resistance in the thermal network, the calculated results are summarized in Table 3.

In order to validate the model, an experimental investigation was made. Using the temperature controller the source temperature was increased 10 °C every 8 min from room temperature (25 °C) to 250 °C and was maintained at each temperature for 2 min during measurement. During this 2 min period no fluctua-
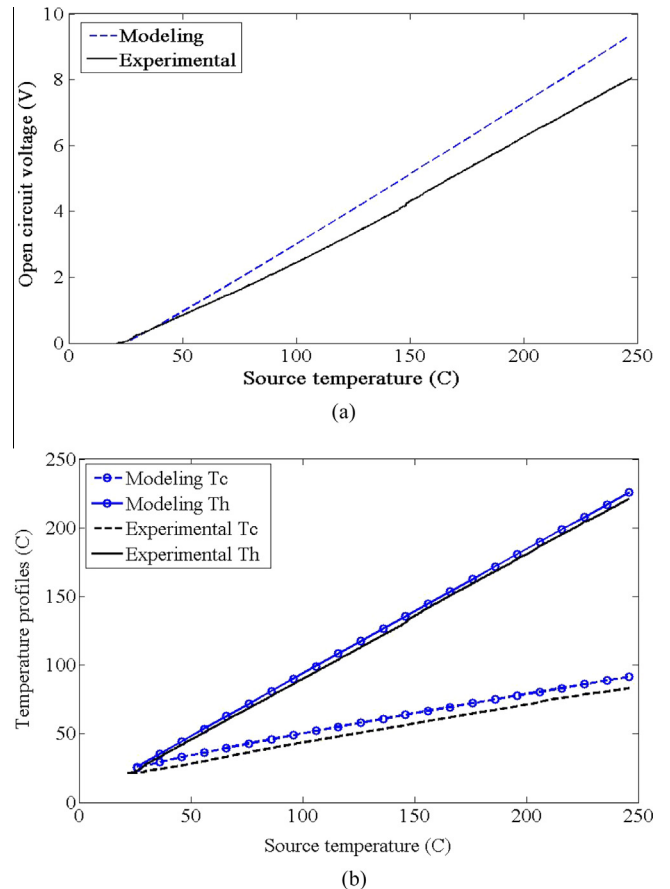
tion in temperature was seen at the cold sides of TEGs, and, since the system is of small size and high thermal conductance, the response time for temperature changes was small. From these observations, steady state was assumed for modeling purposes. Open circuit voltages of each TEM, the match load voltages, total power output, and temperature differences across each TEM under different source temperatures were measured under identical conditions. An external load of $7.9\,\Omega \pm 0.39\,\Omega$ was connected serially with the TEMs to measure power produced under matched load.

Fig. 5 shows the predicted and measured open circuit voltage, hot side temperature, and cold side temperature in terms of source temperature. According to the experimental results, open circuit voltage increases almost linearly with the source temperature. A

Table 3
Calculated values of thermal resistances in the thermal network.

Thermal network items	Calculated values (K/W)
R_s (brass block)	0.064
R_b	0.002
R_{sp}	0.038
R_f (25–250 °C)	2.22–1
Averaged R_{hp} (25–250 °C)	0.035
R_p	0.014
R_{tg}	0.01–0.06
$1/K_{ce}$	2.12
$1/nK_{PN}$ (n = 194)	2.81
$1/K_{los}$ (25–250 °C)	32.15–9.17

Fig. 5. (a) Open circuit voltage vs. source temperature; (b) temperature profile in the open circuit case.
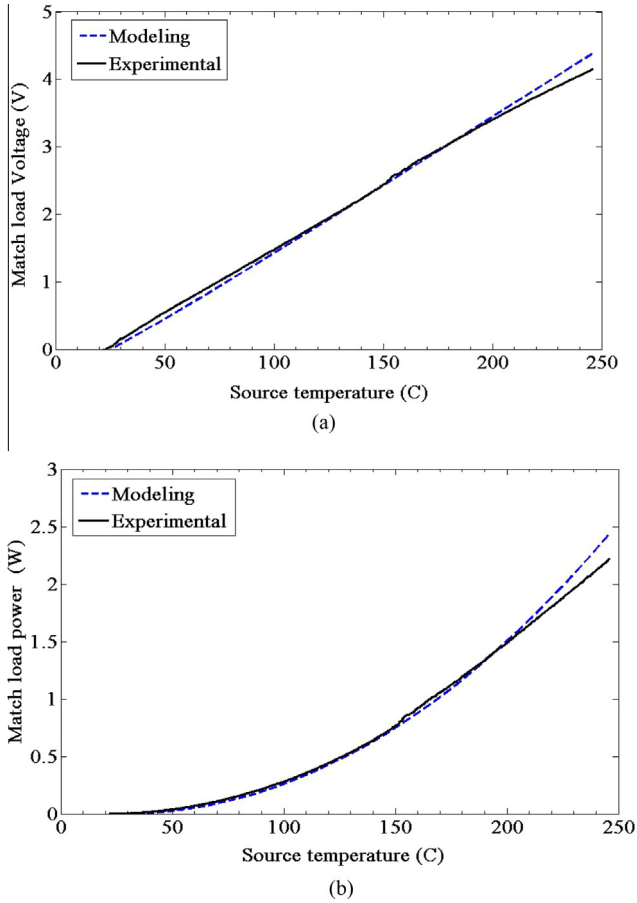
Fig. 6. Match load voltage (a) and power (b) generation at $R_L = 7.9\,\Omega$ vs. source temperature.

Table 4
Case study summary in different external loads and temperature.

	$T_s = 50\,°C$	$T_s = 98\,°C$	$T_s = 146\,°C$	$T_s = 194\,°C$
Analytical modeling	Case 1	Case 2	Case 3	Case 4
Experimental	Case 5	Case 6	Case 7	Case 8

taken both experimentally and analytically within a temperature range of 50–194 °C. Each case is summarized in Table. 4, and results are shown in Fig. 7. Produced voltage increases and current decreases as the external load increases. Thus, maximal power is achieved at match load in each case. As can be seen from experimental results in (c), the impedance of each TEG increases as the source temperature increases, since the point at which maximal power is obtained shifts from 4 Ω to 7.5 Ω as temperature rises. The maximal efficiency and power are achieved at different resistances in the same case, which suggests the power and efficiency have different dependency on external loads. The maximum possible efficiency as predicted by this simulation is 1.33% with an external load of 10 Ω.

The predicted voltage and current curves have 7% error in high resistance range, while the power curve has a larger error of about 15%. This is partially because the electrical resistance is modeled as a constant rather than a temperature dependent parameter. It can be reasoned by the change in the property parameters. The reversed effect of electrical loads on the temperature difference is shown in Fig. 8, where a higher external load connecting to the system yields a higher temperature difference across the module. The external load induced temperature difference is 7.6 °C at $T_s = 194\,°C$ according to the modeling result, which accounts for 9% of the temperature difference.

To verify the effectiveness of the heat pipe in this work, a comparison study was carried out, in which an aluminum rod was used as a substitute for the heat pipe in the assembly. This rod, made of 6061 aluminum has a thermal conductivity of 167 W/m K and was fabricated with the same geometry and surface roughness as the heat pipe so that similar thermal contact resistance could be assumed. Applying the same experimental heating process, the open circuit and match load voltage of both the heat pipe-assisted system and aluminum pipe baseline system is shown in Fig. 9. It is obvious that the use of a heat pipe increased the open circuit, and match load voltage by 2.5 times simultaneously. By utilizing a phase change process, the thermal resistance within the same volume is reduced by more than 87 times, and the overall system resistance is reduced by more than 2.4 times, enhancing the heat flux and power generation by about 6 times.

To examine the impact of sealing material on the system's output, something generally over-looked, a simulation study of system outputs in terms of the sealing material's thermal conductivity was conducted. The thermal conductivity of the sealing material was varied from 0 to 2.0 W/(m K).

Shown in Fig. 10 are the results, where (a) gives the system efficiency, and (b) shows the net thermal resistance change over the target temperature range. From (a), one can see a lower thermal conductivity yields higher temperature difference and therefore higher efficiency, since the sealing material is modeled as a thermal resistor parallel to the P/N legs. As the thermal conductivity of the sealing material rises, the efficiency drops from 2.9% to 1.22%. The black dashed line depicts the thermal conductivity of sealing material in the used TEMs. From (b), the thermal resistance of a single heat sink changes from 2.3 to 1.12, which results in a net change of the overall thermal resistance by about 23%. Both of these effects have large
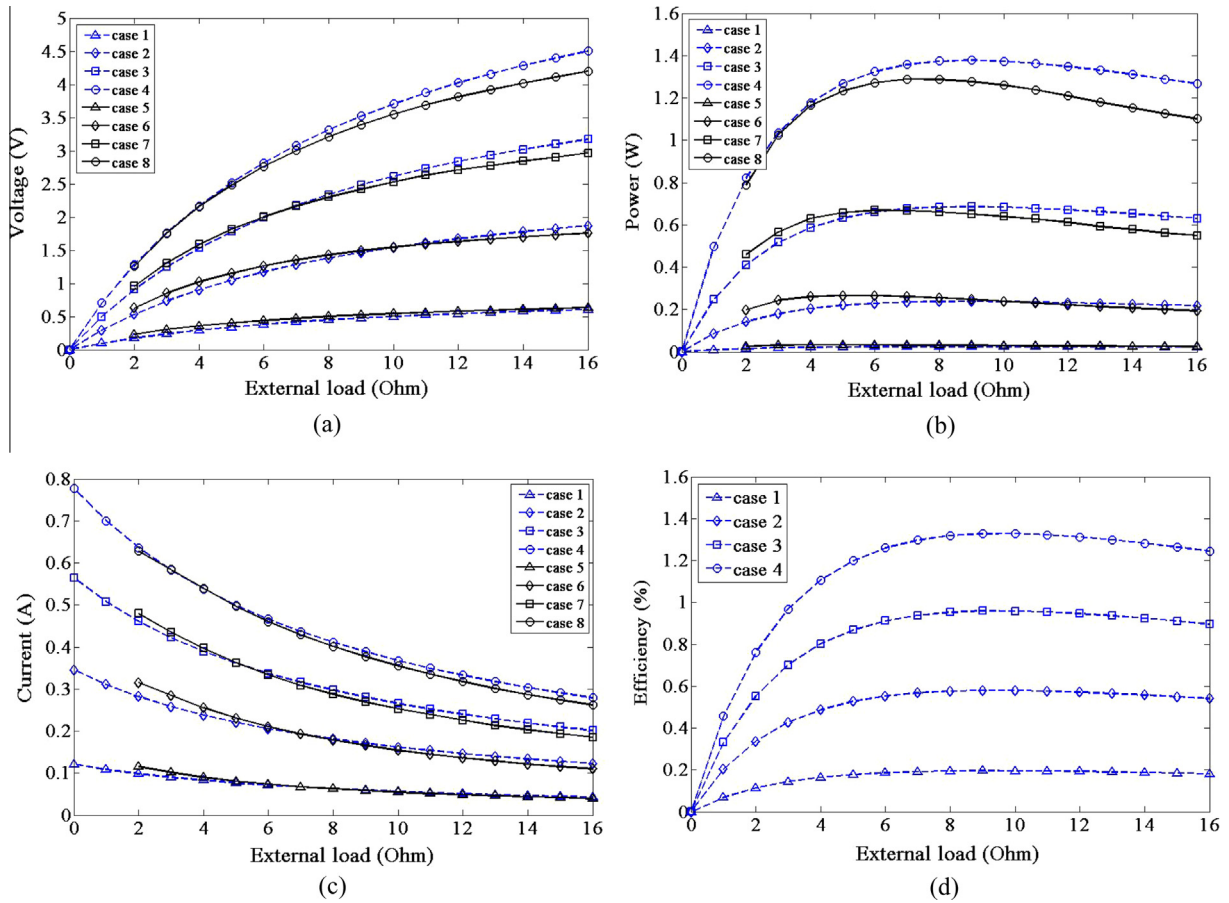
maximum open circuit voltage of 8.06 V ± 0.007 V is achieved at an average temperature difference of 136.9 °C ± 1.12 °C between two modules, and a source temperature of 247.7 °C ± 1.91 °C. Shown in the Fig. 6, the match load voltage and corresponding power increase with the source temperature and reach maximum values of 4.15 V ± 0.007 V and 2.25 W ± 0.13 W, respectively at a source temperature of 246 °C ± 1.9 °C and an average temperature difference of 130 °C ± 1.07 °C.

Shown in Fig. 5, the analytical model predicts an open circuit voltage of 9.29 V at 247 °C, with an error of 13.5% as compared to the experimental result. The error within the temperature profile (average 3% in temperature difference) is lower than that in the open circuit voltage, suggesting the actual Seebeck coefficient is lower than the mean value we used for simulation. From Fig. 6 (a), the modeling and experimental curves of match load voltage overlap in low temperature and have a 5.4% difference at maximum values. Similar results can be seen in the match load power in Fig. 6(b), where a maximal error of 7.6% exists at 246 °C. The reasons for the differences seen in the higher temperature range of both open circuit and match load cases can be caused by: (1) the claimed thermoelectric material properties, such as Seebeck coefficient, being temperature dependent especially at elevated temperature ranges; and (2) The heat loss in high temperature range may not be fully considered.

To analyze the impact of an external load on the voltage, power generation, a resistor box was connected serially with the TEGs, whose resistance was varied from 0 Ω to 16 Ω. Case studies were

Fig. 7. System performance under different external loads and source temperature conditions: (a) voltage; (b) power; (c) current; (d) system efficiency (theoretical analysis).
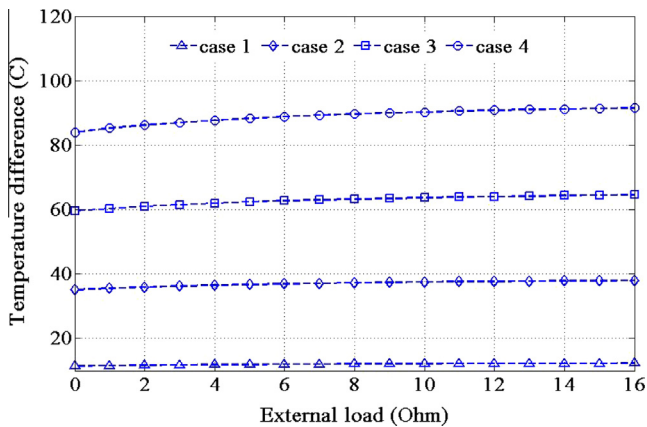

Fig. 8. Effect of external load on heat transfer process (theoretical analysis).

impacts on system, and therefore cannot be neglected in the modeling.

4.2. Real application simulation

After validating the modeling, a real application based simulation was conducted, given the difficulty of setting up a real application experiment. As an example application, the secondary coolant system in a typical Pressurized Water Reactor nuclear power plant is considered. The input parameters and pipe geometry used are listed in Table 5.

An external load of 7.9 Ω is assumed when calculating the match load power. The temperature profile, open circuit voltage, and power estimations are shown in Fig. 11.

From Fig. 11(a), the temperature profiles of both hot and cold side temperatures are estimated based on the conditions in the PWR. Since the fluid in a PWR secondary loop is steam, an equivalent thermal resistance induced by convection, 0.573 °C/W is added. This effectively limits the hot side temperature of TEMs to be less than 250 °C which results in a small reduction in voltage and power generation, as is shown in Fig. 12(b). The maximum voltage and power for this application are 9.7 V, and 2.45 W respectively.

4.3. System level optimization

A simulation of the design was carried out based on the PWR coolant loop application in order to optimize different parameters. The source temperature was assumed to be 250 °C, and the ambient temperature was fixed at 25 °C. The heat loss is neglected in this optimization.

Fig. 12 shows the influence of the number of thermoelectric modules on the system power generation. In (a), as the pair number increases, the peak power generated reaches a maximum at N = 3. By adding more modules, the overall thermal resistance of the combined modules, R_{tem}, is reduced, which leads to a decrease in temperature difference, quickly counterbalancing any increase in voltage output. The curves shift to low current range gradually as N increases primarily because the internal electrical resistance increases linearly with module number. The peak power in each
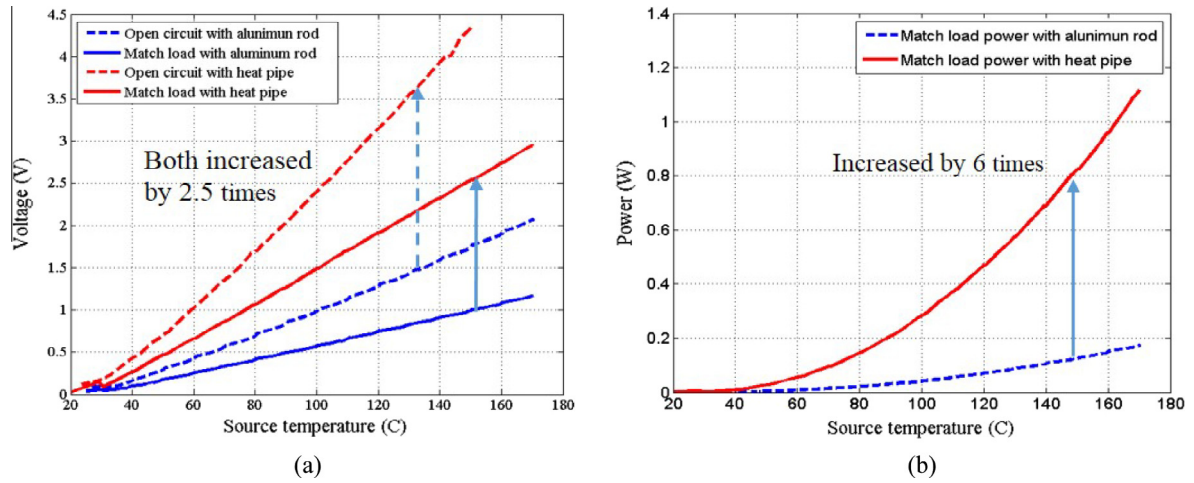
Fig. 9. Comparison study of system performance of both heat pipe assembly setup and baseline setup: (a) open circuit and match load voltage and (b) match load power.
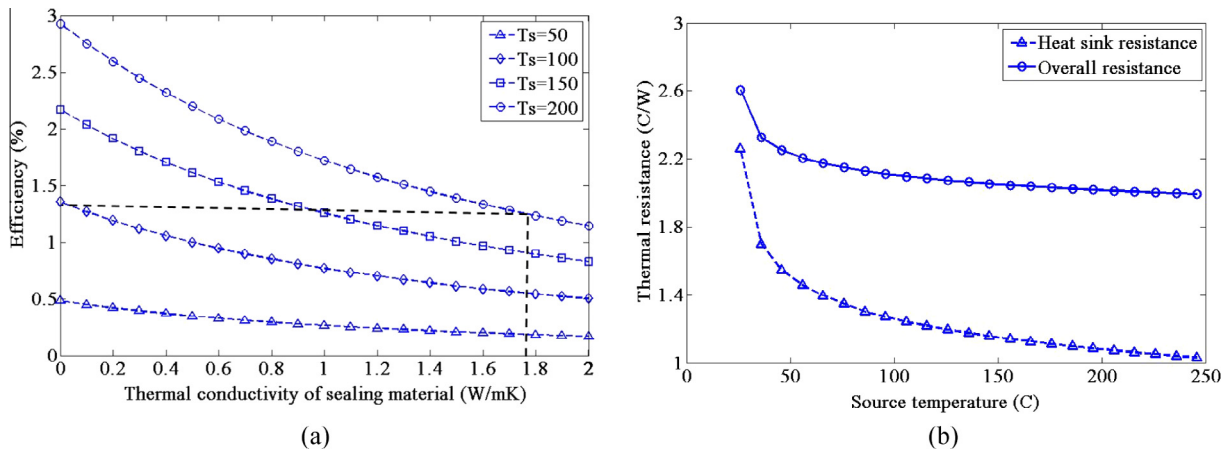

Fig. 10. Sealing material's influence on system outputs: (a) system efficiency (theoretical analysis); (b) thermal resistance change vs. source temperature (theoretical analysis).

Table 5
Input parameters for real application simulation at secondary loop [34].

Parameter item	Value
Outer diameter of steam pipe (m) [34]	0.5
Fluid velocity (m/s) [34]	115
Ambient temperature (°C)	25
Temperature range (°C) [34]	About 275–295
Pressure (bar)	76
Thermal conductivity (W/m K)	0.0652
Dynamic viscosity (Pa s)	1.925×10^{-5}
Specific heat capacity (kJ/kg K)	5.591

case is achieved when the external load matches the internal resistance.

A similar trend for system efficiency is shown in (b), with the notable difference being that the maximum system efficiency is achieved at N = 2. This also shows both maximum efficiency and power cannot be achieved simultaneously in the current design. The increase in efficiency by adding a second pair is only 0.2%, thus, from the prospective of efficiency, using two modules (1 pair) is sufficient.

5. Conclusions

In this work, a thermoelectric generator for harvesting energy from pipelines has been constructed, tested, and modeled. The proposed model accurately estimates the power generation with an error less than 8% in the whole temperature range. The impacts of the TEG sealing material and heat sinks on the system outputs have been investigated, and it has been concluded that both the sealing material and the heat sink have considerable impact on the integrated system performance. The prototype was able to generate a maximum open circuit voltage of 8.06 V ± 0.007 V at a temperature difference of 136.9 °C, and a maximum power of 2.25 W ± 0.13 W at a source temperature of 246 °C ± 1.9 °C using two 1.1″ × 1.1″ TE modules. The innovative use of a heat pipe in this design boosted the power output by 6 times over a design using a simple aluminum rod. Finally, an optimization has been applied to the current design, in which the effects of the module number, and the thermal conductance at both hot and cold ends of the system were studied. It is shown that by adding another pair of TEMs the power generation can be increased by about 50%.
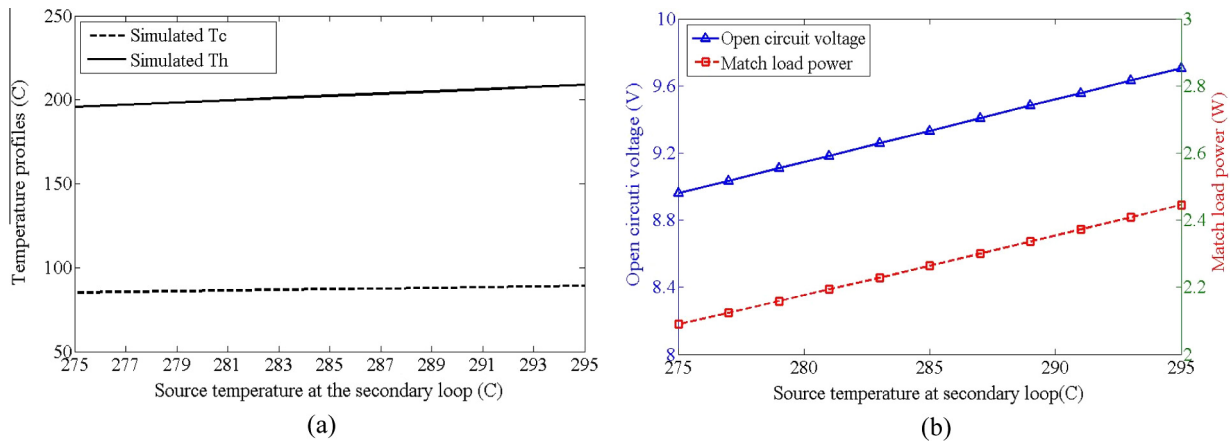
Fig. 11. System outputs in real application (theoretical analysis): (a) system temperature profile; (b) system voltage & power outputs.
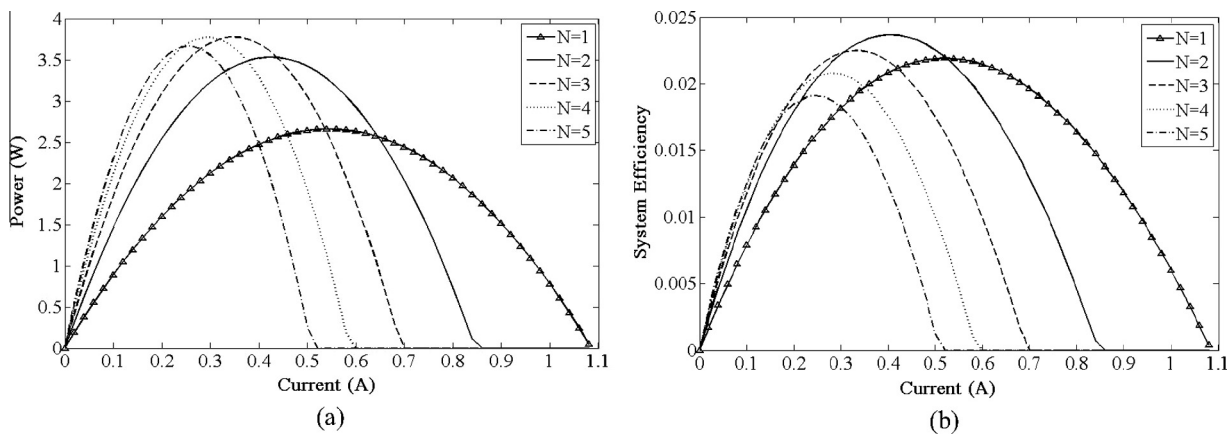

Fig. 12. Effect of module pair number on the power (a) and system efficiency (b) vs. current.

References

[1] Riffat SB, Ma XL. Thermoelectrics: a review of present and potential applications. Appl Therm Eng 2003;23:913–35.
[2] Bahk JH, Fang HY, Yazawa K, Shakouri A. Flexible thermoelectric materials and device optimization for wearable energy harvesting. J Mater Chem C 2015;3:10362–74.
[3] Amatya R, Ram RJ. Solar thermoelectric generator for micropower applications. J Electron Mater 2010;39:1735–40.
[4] Longtin JP, Zuo L, Hwang D, Fu GS, Tewolde M, Chen YK, et al. Fabrication of thermoelectric devices using thermal spray: application to vehicle exhaust systems. J Therm Spray Techn 2013;22:577–87.
[5] Neild AB. Portable thermoelectric generators. SAE Technical Paper; 1963.
[6] Haidar JG, Ghojel JI. Waste heat recovery from the exhaust of low-power diesel engine using thermoelectric generators. In: 2001 Proceedings ICT 2001 XX international conference on thermoelectrics, IEEE 2001. p. 413–8.
[7] Ikoma K, Munekiyo M, Furuya K, Kobayashi M, Izumi T, Shinohara K. Thermoelectric module and generator for gasoline engine vehicles. In: 1998 Proceedings ICT 98 XVII international conference on thermoelectrics, IEEE. p. 464–7.
[8] Hsu CT, Yao DJ, Ye KJ, Yu B. Renewable energy of waste heat recovery system for automobiles. J Renew Sustain Energy 2010;2.

[9] Hsu CT, Huang GY, Chu HS, Yu B, Yao DJ. Experiments and simulations on low-temperature waste heat harvesting system by thermoelectric power generators. Appl Energy 2011;88:1291–7.
[10] Goncalves L, Martins J, Antunes J, Rocha R, Brito FP. Heat-pipe assisted thermoelectric generators for exhaust gas applications. In: ASME 2010 international mechanical engineering congress & exposition. p. 1387–96.
[11] Martins J, Brito FP, Goncalves L, Antunes J. Thermoelectric exhaust energy recovery with temperature control through heat pipes. SAE Technical Paper 2011-01-0315; 2011.
[12] Dell R, Unnthorsson R, Wei CS, Sidebotham GW, Jonsson MT, Foley W, et al. International mechanical engineering congress and exposition – 2012 2013;6 (Pts a and B):635–42.
[13] Tewolde M, Lin CC, Tao H, Chen HF, Fu GS, Liu D, et al. Sensors for small modular reactors powered by thermoelectric generators. In: Proceedings of the ASME small modular reactors symposium.
[14] Zhao DL, Tan G. A review of thermoelectric cooling: materials, modeling and applications. Appl Therm Eng 2014;66:15–24.
[15] Fraisse G, Ramousse J, Sgorlon D, Goupil C. Comparison of different modeling approaches for thermoelectric elements. Energy Convers Manage 2013;65:351–6.
[16] Priya S, Inman DJ. Energy harvesting technologies. Springer; 2009. p. 330.
[17] Chen LG, Gong JZ, Sun FR, Wu C. Effect of heat transfer on the performance of thermoelectric generators. Int J Therm Sci 2002;41:95–9.
[18] Chen JC, Yan ZJ, Wu LQ. The influence of Thomson effect on the maximum power output and maximum efficiency of a thermoelectric generator. J Appl Phys 1996;79:8823–8.
[19] Sahin AZ, Yilbas BS. The thermoelement as thermoelectric power generator: effect of leg geometry on the efficiency and power generation. Energy Convers Manage 2013;65:26–32.
[20] Chen LG, Li J, Sun FR, Wu C. Performance optimization of a two-stage semiconductor thermoelectric-generator. Appl Energy 2005;82:300–12.
[21] Hsiao YY, Chang WC, Chen SL. A mathematic model of thermoelectric module with applications on waste heat recovery from automobile engine. Energy 2010;35:1447–54.
[22] Gou XL, Xiao H, Yang SW. Modeling, experimental study and optimization on low-temperature waste heat thermoelectric generator system. Appl Energy 2010;87:3131–6.

[23] He W, Su Y, Riffat S, Hou J, Ji J. Parametrical analysis of the design and performance of a solar heat pipe thermoelectric generator unit. Appl Energy 2011;88:5083–9.

[24] Hz-2 datasheet. Hi-Z Technology, Inc, <http://www.hi-z.com/uploads/2/3/0/9/23090410/hz-2.pdf> [accessed 16.05.18].

[25] Reay D, McGlen R, Kew P. Heat pipes: theory, design and applications. Butterworth-Heinemann; 2013. p. 31–52.

[26] Rohsenow WM. A method of correlating heat transfer data for surface boiling of liquids. Cambridge (Mass.): MIT Division of Industrial Cooporation; 1951.

[27] Brito FP, Martins J, Goncalves LM, Sousa R. Modelling of thermoelectric generator with heat pipe assist for range extender application. IEEE Ind Elec 2011.

[28] Yovanovich M, Marotta E. Thermal spreading and contact resistances. Heat Transf Handbook 2003;1:261–394.

[29] Guitart Corominas J. Heat sink analytical modelling; 2010.

[30] Culham JR, Yovanovich MM, Lee S. Thermal modeling of isothermal cuboids and rectangular heat sinks cooled by natural-convection. IEEE T Compon Pack A 1995;18:559–66.

[31] Rohsenow WM, Hartnett JP, Cho YI. Handbook of heat transfer. New York: McGraw-Hill; 1998.

[32] Lineykin S, Ben-Yaakov S. Modeling and analysis of thermoelectric modules. IEEE T Ind Appl 2007;43:505–12.

[33] Bitschi A. Modelling of thermoelectric devices for electric power generation. Diss., Eidgenössische Technische Hochschule ETH Zürich, Nr. 18441, 20092009.

[34] Testa D, Kunkle A. The Westinghouse pressurized water reactor nuclear power plant. Westinghouse Electric Corporation Water Reactor Divisions; 1984.